NeuroImage 195 (2019) 373–383

Contents lists available at ScienceDirect

NeuroImage

journal homepage: www.elsevier.com/locate/neuroimage

DeepQSM - using deep learning to solve the dipole inversion for quantitative susceptibility mapping

Steffen Bollmann [a,*], Kasper Gade Bøtker Rasmussen [b], Mads Kristensen [b], Rasmus Guldhammer Blendal [b], Lasse Riis Østergaard [b], Maciej Plocharski [b], Kieran O'Brien [a,c], Christian Langkammer [d], Andrew Janke [a,1], Markus Barth [a,1]

[a] Centre for Advanced Imaging, The University of Queensland, Building 57 of University Dr, St Lucia, QLD, 4072, Brisbane, Australia
[b] Department of Health Science and Technology, Aalborg University, Fredrik Bajers Vej 7, 9000, Aalborg, Denmark
[c] Siemens Healthcare Pty Ltd, Brisbane, Australia
[d] Department of Neurology, Medical University of Graz, Auenbruggerplatz 22, 8036, Graz, Austria

ARTICLE INFO

Keywords:
Quantitative susceptibility mapping
Dipole inversion
Ill-posed problem
Deep learning

ABSTRACT

Quantitative susceptibility mapping (QSM) is based on magnetic resonance imaging (MRI) phase measurements and has gained broad interest because it yields relevant information on biological tissue properties, predominantly myelin, iron and calcium *in vivo*. Thereby, QSM can also reveal pathological changes of these key components in widespread diseases such as Parkinson's disease, Multiple Sclerosis, or hepatic iron overload. While the ill-posed field-to-source-inversion problem underlying QSM is conventionally assessed by the means of regularization techniques, we trained a fully convolutional deep neural network - DeepQSM - to directly invert the magnetic dipole kernel convolution. DeepQSM learned the physical forward problem using purely synthetic data and is capable of solving the ill-posed field-to-source inversion on *in vivo* MRI phase data. The magnetic susceptibility maps reconstructed by DeepQSM enable identification of deep brain substructures and provide information on their respective magnetic tissue properties. In summary, DeepQSM can invert the magnetic dipole kernel convolution and delivers robust solutions to this ill-posed problem.

1. Introduction

Quantitative susceptibility mapping (QSM) is a novel and increasingly utilized post-processing technique that extracts magnetic susceptibility from the phase of magnetic resonance imaging (MRI) gradient echo signal (Deistung et al., 2017; Schweser et al., 2016). Magnetic susceptibility describes the degree of magnetization of a material placed in an external magnetic field and thereby delivers unique, non-invasive insights into tissue composition and microstructure (Deistung et al., 2013; Duyn, 2018). In particular, QSM provides information about myelin and white matter composition (Wharton and Bowtell, 2015; Wu et al., 2017), iron metabolism (Acosta-Cabronero et al., 2016; Langkammer et al., 2012; Schweser et al., 2011; van Bergen et al., 2016; Wang et al., 2017; Yao et al., 2009), and copper accumulation (Fritzsch et al., 2014). The measurement of iron stores has been used to study normal aging (Acosta-Cabronero et al., 2016; Bilgic et al., 2012), Huntington's Disease (van Bergen et al., 2016), Multiple Sclerosis (Eskreis-Winkler et al., 2015; Wisnieff et al., 2015; Zhang et al., 2016), Alzheimer's Disease (Acosta-Cabronero et al., 2013) and Parkinson's Disease (Acosta-Cabronero et al., 2017; Langkammer et al., 2016). Furthermore, QSM visualizes micro-bleeds (Liu et al., 2012a) and differentiates them from microcalcifications (Schweser et al., 2010) due to differing magnetic susceptibilities of calcium and iron.

In order to obtain a quantitative susceptibility map, an image is acquired using an MRI sequence where the signal phase is sensitive to local magnetic field changes, such as a gradient-recalled echo (GRE) sequence (Haacke et al., 2004; Haase et al., 1986; Reichenbach et al., 1997). Raw signal phase is unwrapped and magnetic field contributions from outside the object of interest, the so-called background field, are removed. Finally, the inverse problem relating the measured field perturbation to the underlying magnetic susceptibility distribution is solved (Deistung et al., 2017; Schweser et al., 2016). This critical inversion step is ill-posed

* Corresponding author. Centre for Advanced Imaging, Building 57, Research Road, The University of Queensland, St Lucia, QLD, 4072, Australia.
E-mail address: steffen.bollmann@cai.uq.edu.au (S. Bollmann).
[1] Senior authors contributed equally to this work.

https://doi.org/10.1016/j.neuroimage.2019.03.060
Received 8 March 2018; Received in revised form 3 March 2019; Accepted 26 March 2019
Available online 29 March 2019

and can be overcome either by additional measurements in different orientations or by numerical stabilization strategies.

One method utilizing the acquisition of different object orientations with respect to the static magnetic field is known as 'Calculation of susceptibility through multiple orientation sampling' (COSMOS) (Liu et al., 2009; Wharton and Bowtell, 2010). COSMOS requires at least three different orientations to make the field-to-susceptibility problem over-determined and solves the inverse problem analytically. Although COSMOS generates susceptibility maps of high fidelity, and is therefore considered as gold standard, it assumes isotropic magnetic susceptibility and contains little information about anisotropic tissues (Li et al., 2012; Schweser et al., 2012). Therefore, methods such as susceptibility tensor imaging (STI) (Liu, 2010) or the Generalized Lorentzian Tensor Approach (GLTA) have been developed that extend the magnetic susceptibility scalar to a tensor. To allow the comparison to single-orientation data, the off-diagonal tensor elements of the STI solution are assumed negligible, and the diagonal term (STI33) can be used as an alternative to COSMOS. Common to all multi-orientation methods is their clinical in-feasibility due to patient discomfort and scan time requirements (Deistung et al., 2017; Langkammer et al., 2018). To overcome these practical limitations, a variety of methods have been developed that compute magnetic susceptibility from single orientation data by employing numerical stabilization techniques.

Numerical strategies can be subdivided into two groups (Schweser et al., 2016): inverse filtering and iterative methods. Inverse filtering formulates the problem in Fourier domain where dividing the pre-processed phase data by the unit dipole response yields the magnetic susceptibility. However, near-zero values in the unit dipole response result in an amplification of noise and errors - a manifestation of the ill-posed problem. The unit dipole response is therefore modified and small values are replaced by a fixed threshold. This method is known as truncated k-space division (TKD) (Shmueli et al., 2009; Wharton et al., 2010). Due to the now inaccurate model, TKD parameters need to be carefully chosen to yield a trade-off between regularization and artifacts and TKD results need to be corrected for underestimating magnetic susceptibility (Schweser et al., 2016).

Alternatively, the inverse problem can be solved iteratively in the spatial domain (Schweser et al., 2016). Such iterative numerical solvers require the description of the forward solution (the multiplication of the dipole kernel with the susceptibility distribution in Fourier space) and they minimize the difference between this predicted data and the actual data in a least-squares sense. One example to solve this equation system is the LSQR algorithm (Li et al., 2015; Paige and Saunders, 1982). Most recent QSM inversion algorithms are extensions to this basic principle and only differ in the way how regularization techniques incorporate prior information about the susceptibility distribution. Common to all techniques is that the regularization has to be carefully optimized to yield a trade-off between data and priors (Liu et al., 2012b; Schweser et al., 2016). Morphology enabled dipole inversion (MEDI) is a spatially regularized inversion that utilizes edge information from magnitude images to regularize the problem (Liu et al., 2013, 2011). Other methods are total generalized variation (TGV) (Langkammer et al., 2015), or single-step QSM (SS-QSM) (Chatnuntawech et al., 2017). Common to all iterative methods is that the forward solution has to be evaluated at least once in every iteration step. This then leads to the fact that the forward solution cannot be computationally expensive in order to be evaluated iteratively to solve the inverse problem.

Recently, deep neural networks have emerged as an alternative to iterative methods for solving inverse problems (Fan et al., 2017; Jin et al., 2017; McCann et al., 2017; Shen et al., 2017), and have shown impressive results in applications such as denoising (Burger et al., 2012), deconvolution (Xu et al., 2014), image reconstruction (Golkov et al., 2016; Schlemper et al., 2017; Zhu et al., 2018) and super-resolution (Bahrami et al., 2017; Kim et al., 2016; McDonagh et al., 2017; Oktay et al., 2016). The use of neural networks for the solution of inverse problems is motivated by the fact that neural networks are capable of approximating any continuous function under the assumption that the network has enough free parameters (Hornik, 1991; McCann et al., 2017; Shen et al., 2017). Researchers have also investigated the link between iterative methods and deep networks and found that neural networks act as a fast approximated sparse coder (Gregor and LeCun, 2010; Jin et al., 2017). A sparse coder learns the most important features from the input data and can reconstruct the input using a combination of basis vectors (Gregor and LeCun, 2010). It has been shown (Jin et al., 2017) that the reconstructed images from the neural network preserved complex textures better than the state of the art iterative methods, because the neural network learns an efficient regularization from the data, whereas iterative methods require explicit regularization. An important practical advantage of neural networks over iterative methods is that the trained models can produce an output extremely fast as they only involve a single step of matrix multiplications to produce the feed forward output (McCann et al., 2017). In addition, it has already been suggested (Anderson et al., 2016) that the QSM inversion can be optimized by only including relevant field contributions in the inversion process, which could be achieved by tailoring a U-Net filter architecture to the physics requirements of the dipole field.

Based on the recent advances in the solution of inverse problems using deep learning, we propose a deep convolutional network that delivers fast and accurate solutions to the ill-posed field-to-source problem. We test the generalisability in three separate experiments with increasing complexity: The first experiment tests the performance on a dataset very similar to the training data. The second experiment goes one step further and tests how the inversion works for *in vivo* phase data where a COSMOS and STI33 reconstruction is available as a comparison. The third experiment investigates the network's real-world performance on a high-resolution brain dataset acquired at 7 T from 27 healthy individuals. We show that DeepQSM is capable of utilizing single-orientation phase data without the need for explicit regularization terms and manual parameter tweaking and successfully delivers quantitative susceptibility maps.

2. Methods

2.1. Network architecture

The fully convolutional neural network (DeepQSM), capable of processing 3-dimensional inputs, is based on a modified version of an established architecture (U-Net) (Ronneberger et al., 2015). Due to memory constraints on the Graphic Processing Units (GPUs) used for training we reduced the amount of feature-maps compared to the original U-Net; see Fig. 1 for the architecture of DeepQSM. The fully convolutional nature of the chosen architecture allows an input image of any size with dimensions divisible by 16 and the dimensions of the output equal the dimensions of the input.

The architecture can be divided into a contracting and an expanding part. The goal of the contracting part is to capture the context of the image, while the goal of the expanding part is to increase the resolution (Jin et al., 2017). The contracting part of DeepQSM consists of three-dimensional convolution layers with filters of size $3 \times 3 \times 3$, a stride length of $1 \times 1 \times 1$ and rectified linear units (ReLU). Furthermore, pooling layers are added, which both increase the receptive field and make the network translation invariant. The expanding part of the neural network consists of two types of convolutional layers: transposed convolutional layers and convolutional layers. The transposed convolutional layers consist of filters of size $2 \times 2 \times 2$, a stride length of $2 \times 2 \times 2$ and ReLUs. The convolutional layers in the expanding part are identical to the convolutional layers in the contracting part.

The network has so-called skip connections between the contracting and expanding part of the network. The skip connections make up for the spatial information lost during downsampling by combining high resolution information with low resolution information. Furthermore, it reduces the gradient vanishing problem and increases the performance of the network (Jin et al., 2017).

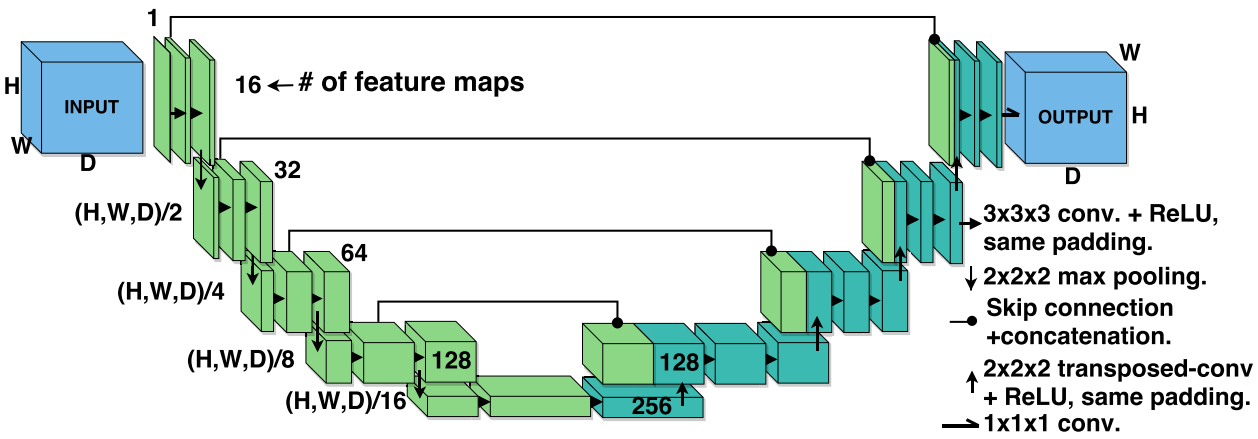

Fig. 1. The DeepQSM architecture consists of a contracting and expanding part. The contracting part is made up of a series of convolutions with a ReLU activation function followed by a pooling layer. The expanding part consists of transposed convolutions to undo the spatial reduction caused by the pooling operations and convolutions with ReLUs similar to those of the contracting part. Convolutions used a stride of $1 \times 1 \times 1$, transposed convolutions a stride of $2 \times 2 \times 2$, pooling a stride of $2 \times 2 \times 2$. DeepQSM will output a volume with identical dimensions to the input.

2.2. Dipole kernel

The dipole kernel commonly used in QSM (Chatnuntawech et al., 2017; Deistung et al., 2017; Liu et al., 2015; Schweser et al., 2016) is built on two assumptions: The first assumption is that the effect of the local environment on susceptibility can be divided into near field and far field based on the Lorentz sphere (Yablonskiy and Sukstanskii, 2015). Under the assumptions that the magnetic susceptibility is a bulk property and that magnetic moments in the near field are randomly distributed, the contribution of the near field can be neglected (Yablonskiy and Sukstanskii, 2015). Equation (1) shows the dipole kernel d in the Fourier domain, where k_x, k_y and k_z are k-space vectors in the respective directions. This dipole description does not include terms for modelling anisotropy:

$$FT(d) = \frac{1}{3} - \frac{k_z^2}{k_x^2 + k_y^2 + k_z^2} \tag{1}$$

2.3. Training procedure

DeepQSM was trained on 100 000 $64 \times 64 \times 64$ synthetic examples in 91600 steps with 40 examples per step resulting in a total training time of 35 h on an NVIDIA Tesla V100 Accelerator Unit. The synthetic 3D images were simulated and contained basic geometric shapes (cubes, rectangles and spheres) and served as label data. The training data contained between 80 and 120 cubes and between 80 and 120 spheres per image. The shape sizes were randomly varied between 10% and 40% of the image size, which was set to $160 \times 160 \times 160$. Every shape was assigned a susceptibility value drawn from a uniform distribution with -0.2 minimum and 0.2 maximum. The shapes were randomly added to the image, which was then convolved with the dipole kernel. Finally, 100 $64 \times 64 \times 64$ patches were randomly extracted from this image for training.

To optimize the weights of DeepQSM during training the 'ADAM' optimizer (Kingma and Ba, 2014) was used, and had the following configurations: initial learning rate = 0.001, $\beta_1 = 0.9$, $\beta_2 = 0.99$. Mean squared error between the reconstruction from DeepQSM and the label data served as the cost function for the optimizer.

To avoid overfitting during training and thereby losing generalisability, the regularization technique 'dropout' was used (Srivastava et al., 2014) to randomly turn off neurons during training with a dropout rate of 5%.

DeepQSM was implemented using Python 3.6.6 (Rossum, 1995), Tensorflow and Tensorboard v1.11.0 (Abadi et al., 2016), Keras 2.2.4 (Francois, 2015), SciPy 1.1.0 (Jones et al., 2001), NumPy 1.15.0 (Oliphant, 2015), scikit-image 0.13.1 (Walt et al., 2014) and Nibabel 2.3.0 (Brett et al., 2018). Matplotlib 2.1.2 (Hunter, 2007) and Seaborn 0.8.1 (Waskom et al., 2017) were used for visualizations and figures in this manuscript. The source code of DeepQSM is available from the authors upon request. Training was performed on the National Computational Infrastructure cluster *Raijin* using NVIDIA Tesla K80 GPUs and on the University of Queensland cluster *Wiener* using NVIDIA Tesla V100 Accelerator units.

We performed three experiments to evaluate DeepQSM's ability to solve the ill-posed field-to-source inversion. As a comparison to DeepQSM we used two iterative QSM processing pipelines and we reconstructed the same datasets using STI Suite's iLSQR inversion (https://people.eecs.berkeley.edu/~chunlei.liu/software.html) with 150 iterations and optimized parameters and MEDI (Li et al., 2012; Liu et al., 2011) with the optimized parameters for a 7 T human brain dataset (lambda 300; merit 1).

2.4. Experiment 1: synthetic data

The first experiment aimed to test DeepQSM's performance on synthetic data similar to the training data. The goal was to test if DeepQSM would produce sensible outputs on new synthetic data that were simulated exactly the same way as data used for training, then convolved with the dipole kernel to generate a forward solution. Next, DeepQSM was used to invert the applied dipole kernel to reconstruct the simulated susceptibility distributions. The results were compared to the simulated ground truth through the use of difference maps and their histograms and kernel density estimations. The mean of the histogram indicates if there is a consistent bias and the standard deviation indicates the spread of reconstruction errors. We also included numerical error measures, i.e. the normalized root mean-squared error, the mean structural dissimilarity index and the high frequency error norm.

2.5. Experiment 2: QSM reconstruction challenge data

In the second experiment the goal was to solve the ill-posed problem on susceptibility maps from realistic single orientation phase data and compare the reconstruction to COSMOS and STI33. DeepQSM had never been introduced to images of brains during training and therefore this experiment would test if DeepQSM generalized the underlying principle of the QSM dipole inversion. A single orientation background-field-corrected tissue phase image published by Langkammer et al. (2018) from the 2016 QSM reconstruction challenge was used. The dataset serves as a common reference for current and future algorithms and was

acquired *in vivo* from a healthy 30 year old female, using a 3D gradient-echo at 3 T with 1.06 mm isotropic resolution, an echo time of 25 ms and a repetition time of 35 ms (Langkammer et al., 2018).

2.6. Experiment 3: high resolution 7 T in vivo group data

The third experiment aimed to test if DeepQSM can reconstruct QSM images of a real-world healthy volunteer group dataset. For this, we obtained written informed consent from participants prior to *in vivo* scanning as approved by the local human ethics committee. We investigated 27 participants (21–34 years of age, 26.3 years on average, 13 males) on a 7 T whole-body research scanner (Siemens Healthcare, Erlangen, Germany), with maximum gradient strength of 70 mT/m and a slew rate of 200 mT/m/s. A 7 T Tx/32 channel Rx head array (Nova Medical, Wilmington, MA, USA) was used for radio frequency transmission and signal reception. Third order shimming was employed to improve the B_0-field homogeneity.

We acquired 3D GRE whole brain datasets with multiple echo times: TR = 25 ms, TE = 4.4, 7.25, 10.2, 13.25, 16.4, 19.65, 23 ms, flip angle = 13°, FOV = 210 × 181.5 × 120 mm^3, matrix = 280 × 242 × 160 (0.75 mm isotropic voxels), parallel imaging (GRAPPA, acceleration factor = 2, 24 auto-calibration lines), monopolar readout gradient, symmetric echo, 1116 Hz/Pixel, first echo flow compensated, TA = 7.9 min.

To enable optimal coil combination using COMPOSER (Robinson et al., 2017), we acquired reference data using the prototype PETRA ultra-short-TE sequence (Grodzki et al., 2012): TR = 1.99 ms, TE = 0.07 ms, flip angle = 2°, FOV = 288 × 288 × 288 mm^3, matrix = 288 × 288 × 288 (1 mm isotropic voxels), 847 Hz/Pixel, and TA = 2 min.

All pre-processing for the comparison of different inversion algorithms was performed using Nipype 1.1.3 (Gorgolewski et al., 2011), FSL 5.0.9 and STI Suite 2.2 (Li et al., 2015, 2014, 2011). The data were cropped to 224 × 272 × 160 pixels to ensure a matrix size divisible by 16 and a brain mask was generated using *FSL Brain Extraction Tool* (BET) (Smith, 2002) with a fractional intensity threshold of 0.4. Then we used STI Suite's Laplacian-based phase unwrapping and background field correction iHARPERELLA to generate the input to the different inversion algorithms.

For evaluating the group level results, we used an atlas based segmentation of sub-cortical structures, i.e. dentate nucleus, red nucleus, substantia nigra, putamen, globus pallidus and caudate nucleus. The volgenmodel pipeline (Fonov et al., 2011; Grabner et al., 2006; Janke and Ullmann, 2015) was used to construct a minimum deformation model of the GRE magnitude data. First, all 7 echoes were averaged per individual and then the initial target was generated based on one individual dataset blurred using a gaussian kernel size of 4 mm to remove individual features and allow a registration of all individuals to this starting template. Then all original input images were aligned via a 12 parameter affine transformation and a normalized cross correlation objective function. The original input datasets were then resampled to the model space and transformed using a concatenation of the inverse transformation from model to participant space and the average transform. Finally, the next model stage was computed by averaging the resampled data. After the affine transformation, non-linear registration was used with incrementally decreasing step (32, 16, 12, 8, 6, 4, 2, 1 mm) and smoothing kernel (16, 8, 6, 4, 3, 2, 1, 0.5 mm) sizes to register the individual datasets to the evolving group template. The final transformations from participant to atlas space were then applied to the QSM data and averaged across participants to generate the different QSM group templates, as shown in Fig. 5. We manually segmented dentate nucleus, red nucleus, substantia nigra, putamen, globus pallidus and caudate nucleus in the QSM group template using ITK-SNAP (Yushkevich et al., 2006). Susceptibility values of every participant were extracted from all QSM datasets and visualized in Fig. 6 using a box-and-whisker plot. After confirming the assumptions for an analysis of variance (ANOVA), quantitative differences between methods were assessed using one-way ANOVAs with QSM method as a factor implemented via an ordinary least squares framework in the statsmodels python module (Seabold and Perktold, 2010). If the ANOVA per region showed a significant difference, post-hoc tests were performed corrected for multiple comparisons across and within anatomical regions using Tukey's Honest Significant Difference (Tukey, 1949) test with a familywise error rate of 0.05.

3. Results

The following experiments demonstrate the performance of the network trained only on synthetic data and applied to a variety of datasets with increasing complexity. All DeepQSM predictions were computed in approximately 10 s on a standard desktop computer with an i7-4790 CPU and 16 GB of memory.

3.1. Experiment 1: synthetic data

Fig. 2 illustrates the prediction performance of DeepQSM on synthetic data and compares it to the simulated ground truth. This figure illustrates DeepQSM's capability of reverting the effects of the dipole on synthetic data. The difference maps show that remaining errors are mainly in the proximity of edges (especially STI iLSQR and DeepQSM), in square objects (DeepQSM) and a residual slowly varying background field (especially STI ilSQR and MEDI). The histograms and error measures show that DeepQSM's error distribution is centred on 0 indicating that there is no systematic quantification bias and a similar reconstruction error than iLSQR for this dataset. MEDI shows very low error measures for the high frequency error norm and the normalized root mean-squared error.

3.2. Experiment 2: single orientation phase

Figs. 3 and 4 show DeepQSM's ability to reconstruct single orientation phase data. The comparison of the results with iLSQR and MEDI inversions shows that DeepQSM delivers a visually comparable susceptibility map. Further, the comparison of all QSM solutions to STI33 (Fig. 3) and COSMOS (Fig. 4) ground truths shows that no method can achieve the multi-orientation solutions and that methods differ in the amount of streaking artifacts and regional quantification results.

3.3. Experiment 3: high resolution 7 T in vivo group data

The result of experiment 3 can be seen in Figs. 5 and 6 demonstrating how DeepQSM is able to solve the inverse problem on high resolution phase data from a single orientation in a group of 27 participants. This example illustrates that DeepQSM can deliver susceptibility maps from high resolution data without requiring retraining.

4. Discussion

In this proof-of-concept study, we demonstrated that the challenging inverse problem underlying QSM can be solved by using a fully convolutional neural network. We achieved this by computing the well-posed QSM forward solution of synthetic data consisting of simple geometrical shapes, and we trained the network on these inverse and forward solution pairs. The first experiment tested the performance on a dataset very similar to the training data. The network was able to invert this problem, but it could have done this by overfitting the training data. Therefore, the second experiment investigated the network's performance on a real phase dataset from a human brain, containing structures that the network has never seen during training. We used the STI33 and COSMOS reconstructions from the 2016 QSM reconstruction challenge (Langkammer et al., 2018) to evaluate the performance. This showed that the network has learned the general concept of the dipole inversion and not just the shapes presented during training. The third experiment demonstrated that the inversion works with high-resolution *in vivo* phase data in a group of 27 healthy volunteers.

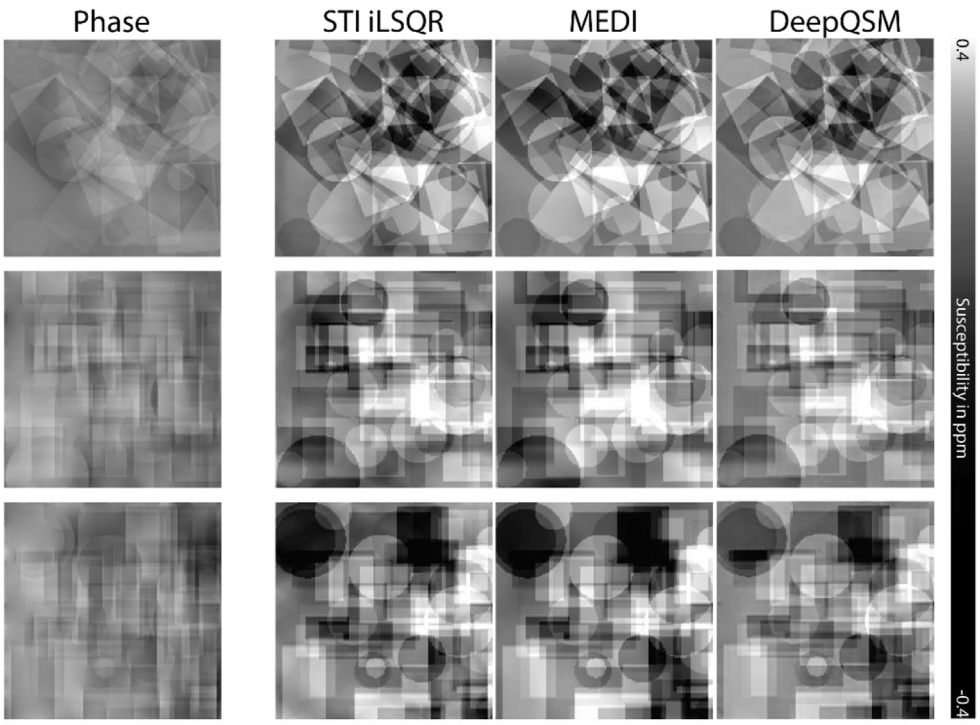

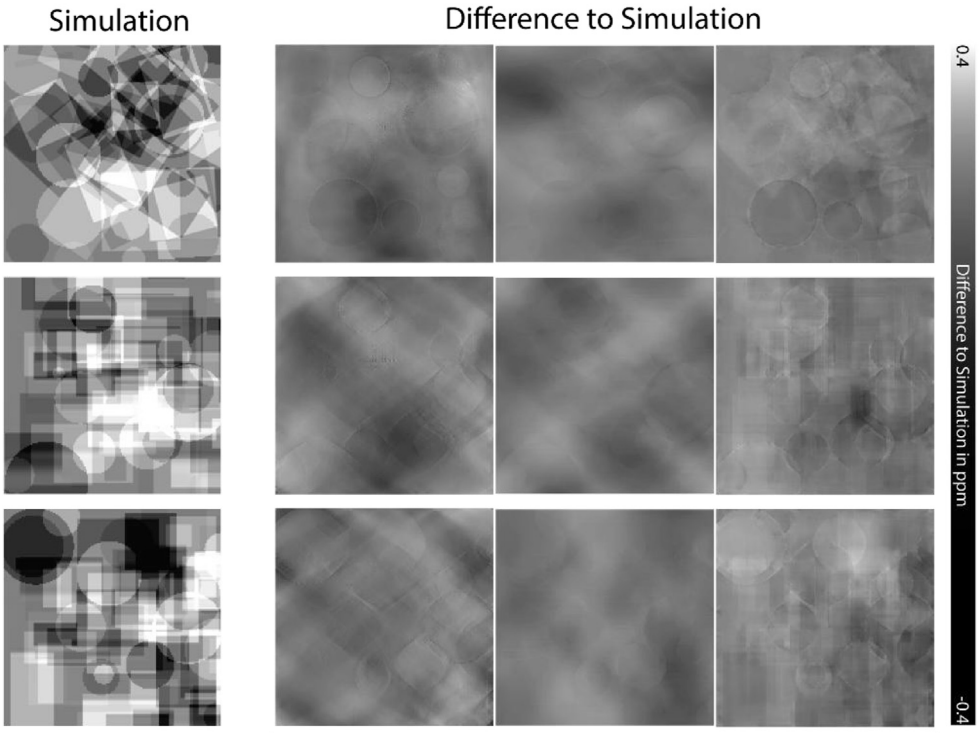

Error Measures

	CHI HFEN	CHI SDSIM	CHI NRMSE
STI	20.67	0.31	39.68
MEDI	9.69	0.27	30.91
DeepQSM	23.69	0.21	41.29

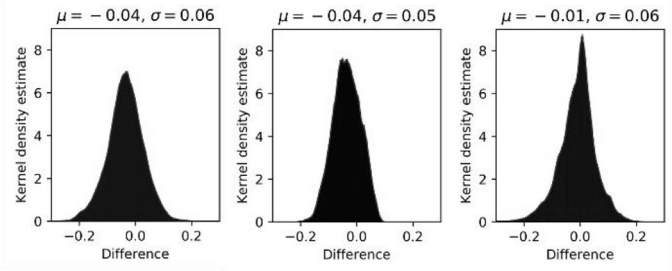

Fig. 2. Comparing the reconstruction of simulated 3D data between STI iLSQR, MEDI and DeepQSM. The simulated dataset was convolved with the dipole kernel and this was then used to reconstruct susceptibility maps with 3 different algorithms. The susceptibility maps were compared with the simulated ground truth by difference maps and histograms of the difference. The difference maps show that all algorithms cannot perfectly recover the true susceptibility distributions and that there are errors in the proximity of edges (particularly in iLSQR and DeepQSM) and a residual slowly varying background field (particularly in iLSQR and MEDI). The histograms and error measures (HFEN=High-Frequency Error Norm, SDSIM=Structural Dissimilarity Index (1-SSIM), NRMSE=Normalized Root Mean-Squared Error) show similar performance levels between all compared methods.

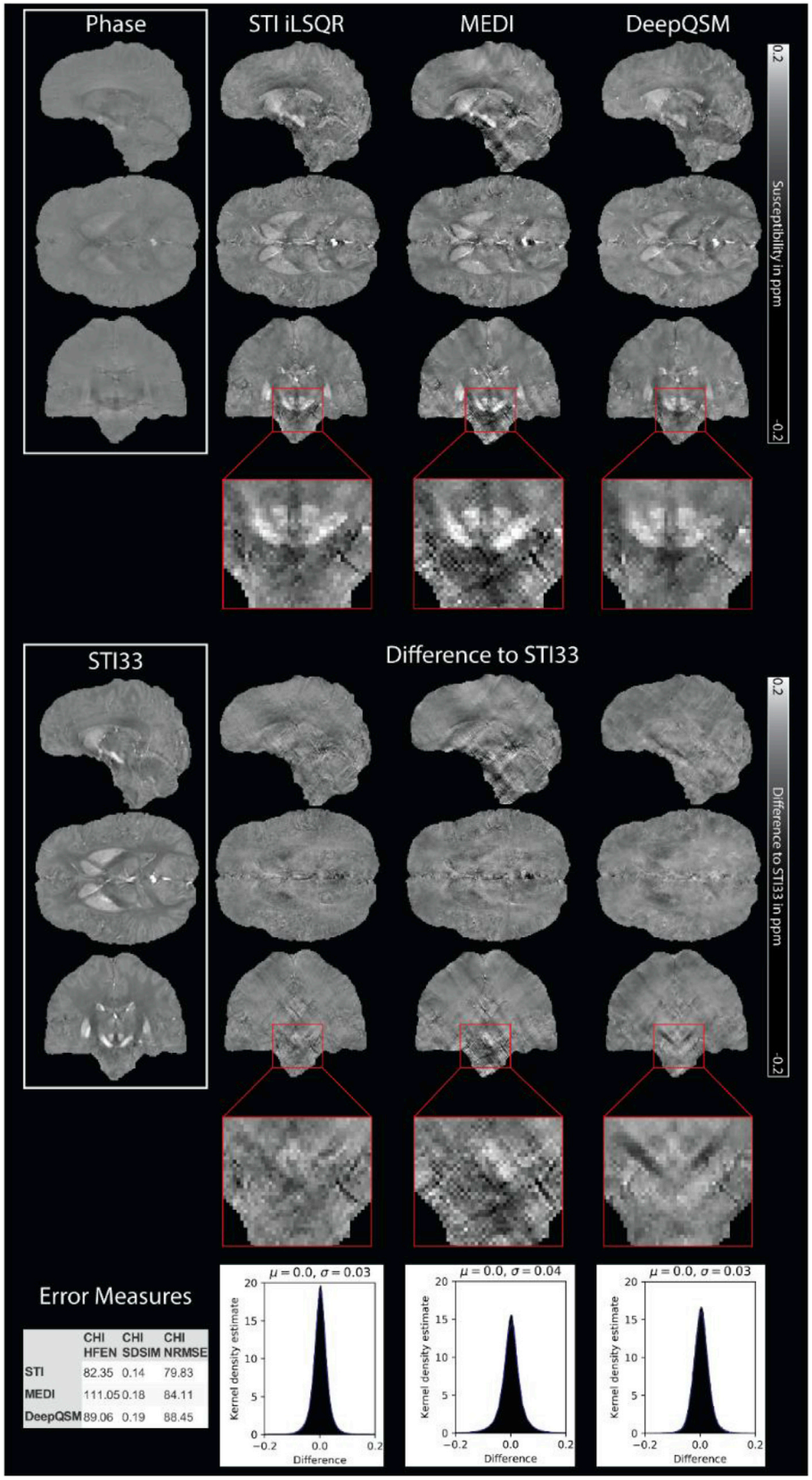

Fig. 3. Sagittal, axial and coronal slices from the 2016 QSM reconstruction challenge single orientation phase dataset (top, left) reconstructed using iLSQR, MEDI and DeepQSM. The bottom half shows the STI33 reconstruction (left) and the difference maps of the susceptibility maps with respect to the STI33 result. The error measures and histograms of the difference maps illustrate that all algorithms deliver comparable quantification results.

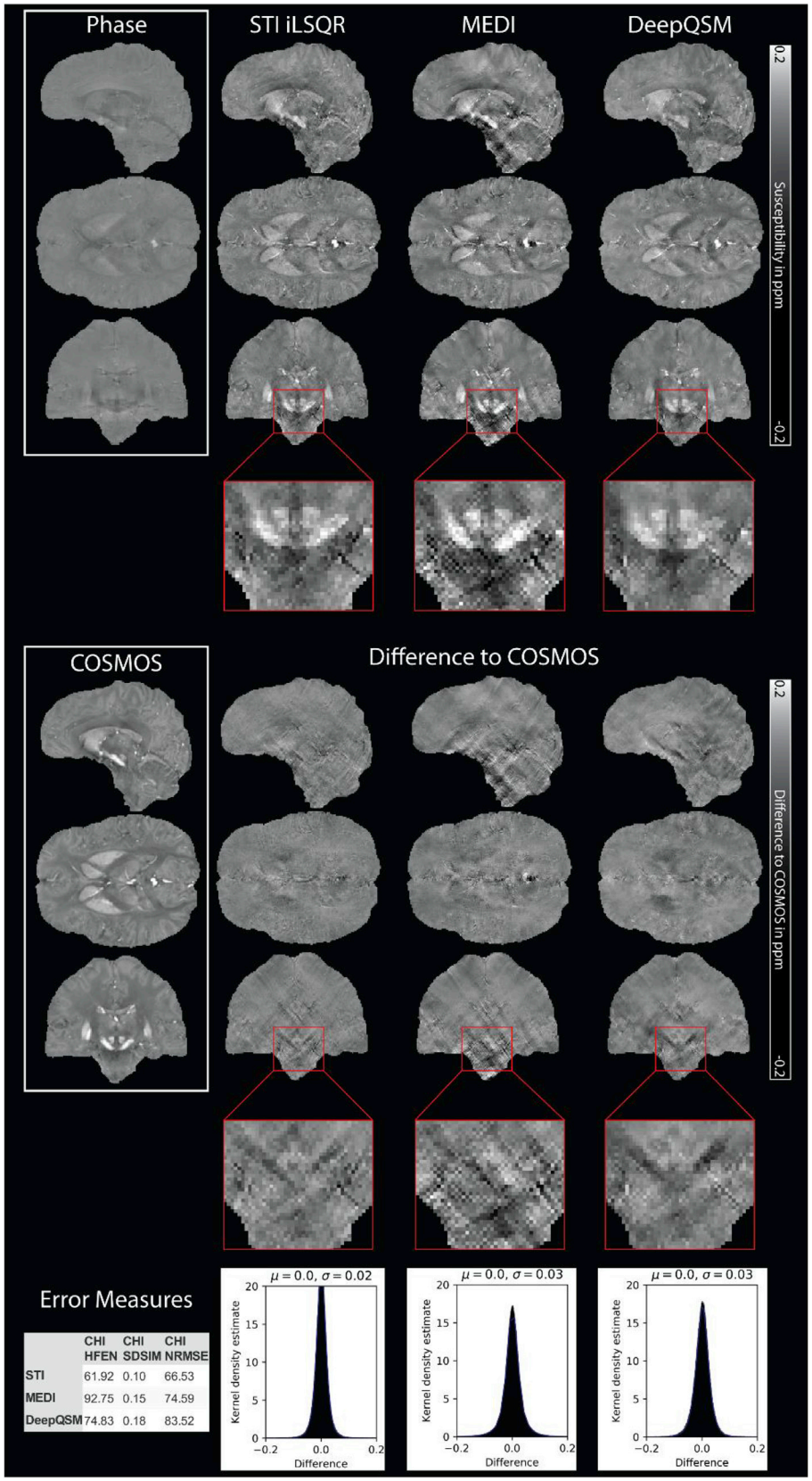

Fig. 4. Sagittal, axial and coronal slices from the 2016 QSM reconstruction challenge single orientation phase dataset (top, left) reconstructed using iLSQR, MEDI and DeepQSM. The bottom half shows the COSMOS reconstruction (left) and the difference maps of the susceptibility maps with respect to the COSMOS result. The error measures and histograms of the difference maps illustrate that all algorithms deliver comparable quantification results.

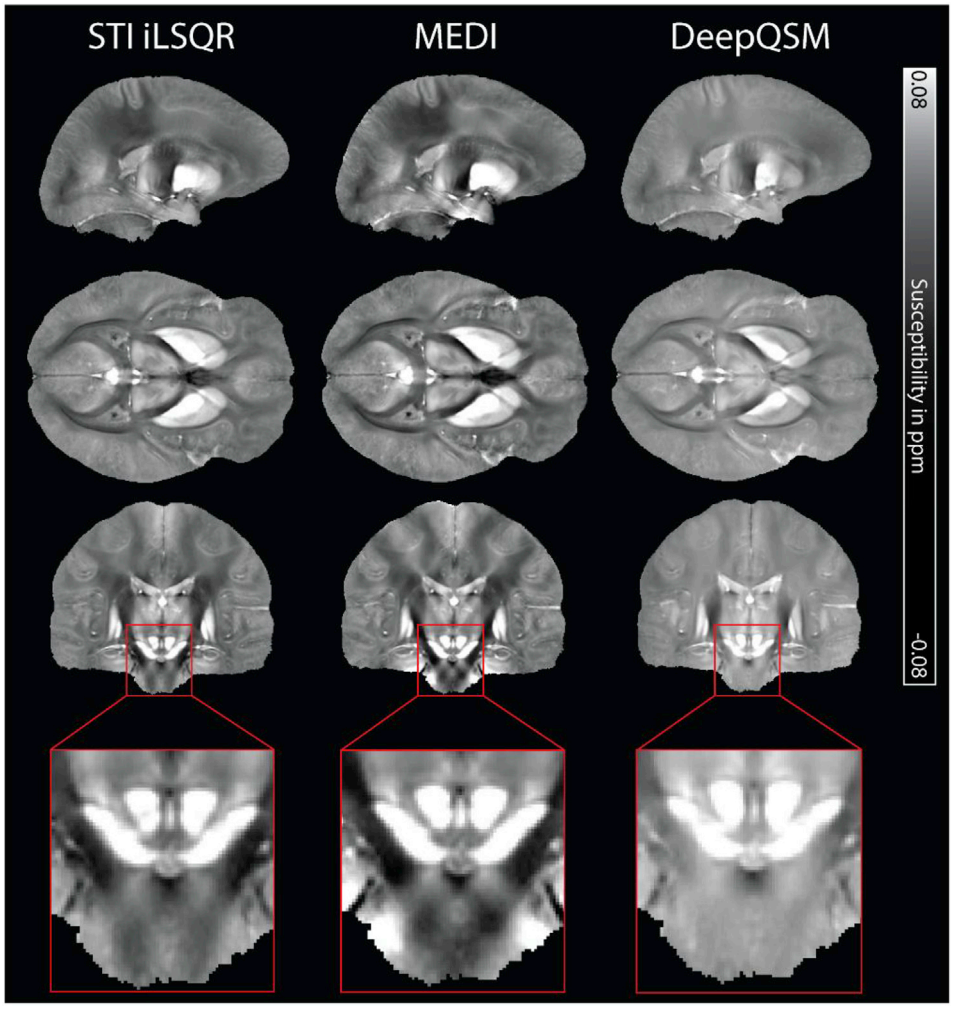

Fig. 5. The iHARPERELLA background field corrected phase was used to reconstruct susceptibility maps using iLSQR, MEDI and DeepQSM. All 27 participants were combined in a group template to investigate group level effects of each method.

We compared the susceptibility reconstructions from DeepQSM with two widely utilized reconstruction methods, namely STI Suite's iLSQR and MEDI. We showed that DeepQSM is capable of delivering robust results without any parameter adjustments, although it was only trained on simple geometrical shapes. The difference maps and histograms of the differences illustrate that DeepQSM has no systematic bias and that the quantitative errors are in the same range as for iLSQR and MEDI.

DeepQSM is currently only trained on simple geometrical shapes. The purpose of this was to test if the network can learn the dipole deconvolution itself, rather than image features of the desired output (e.g. brain anatomy). This shows that our network has learned to approximate the underlying principle of dipole inversion and that training data with anatomical priors, as recently proposed in an approach by Yoon et al. (2018), might not be necessary. In future versions of DeepQSM, we need to characterize the output of the network for a variety of susceptibility configurations and training datasets to understand how an optimal training set would look like. Improvements for the simulated training data could include zero padding around the training datasets before the convolution operation to avoid artifacts close to the edges of the volume. The reason why the quantitative results of different QSM methods differ in some anatomical regions significantly (see Fig. 6, e.g. putamen and globus pallidus) are most likely an interaction between algorithmic properties (e.g. stepwise constant) and geometrical properties of the anatomical structures investigated. Another limitation of DeepQSM is that numerical error measures indicate no better quantitative performance in comparison to iterative procedures. However, the error measures used to assess the quantification accuracy and in particular the available “gold standards” (STI33 and COSMOS) are currently controversial topics in the community. This debate is clearly reflected in the concluding sentence of the recent report on the QSM reconstruction challenge (Langkammer et al., 2018) with input from 13 research groups and several meetings stating “the challenge highlighted the need for better numerical image quality criteria”, which is out of scope of this paper.

Currently, we have used background field corrected data to compute a QSM solution. However, it is also possible to incorporate realistic simulations of background fields originating at tissue boundaries into the training step as shown in the follow-up work of this manuscript (Bollmann et al., 2019). Incorporating the background field correction and the inversion in a single step would then allow the background field removal together with the field-to-source inversion (Heber et al., 2019) in an end-to-end fashion, similar to state of the art iterative single-step QSM algorithms (Langkammer et al., 2015).

In our current implementation, we utilized a simple dipole model with the assumption that magnetic susceptibility is a scalar quantity. An advantage of our proposed approach is that it can potentially utilize any forward model, and as such could incorporate additional model terms accounting for anisotropy of magnetic susceptibility and structural tissue anisotropy. Currently, the inverse problem posed by these more sophisticated models, such as the Generalized Lorentzian Tensor Approach (Yablonskiy and Sukstanskii, 2015), cannot be solved. Thus, a deep learning approach incorporating additional measurements, such as

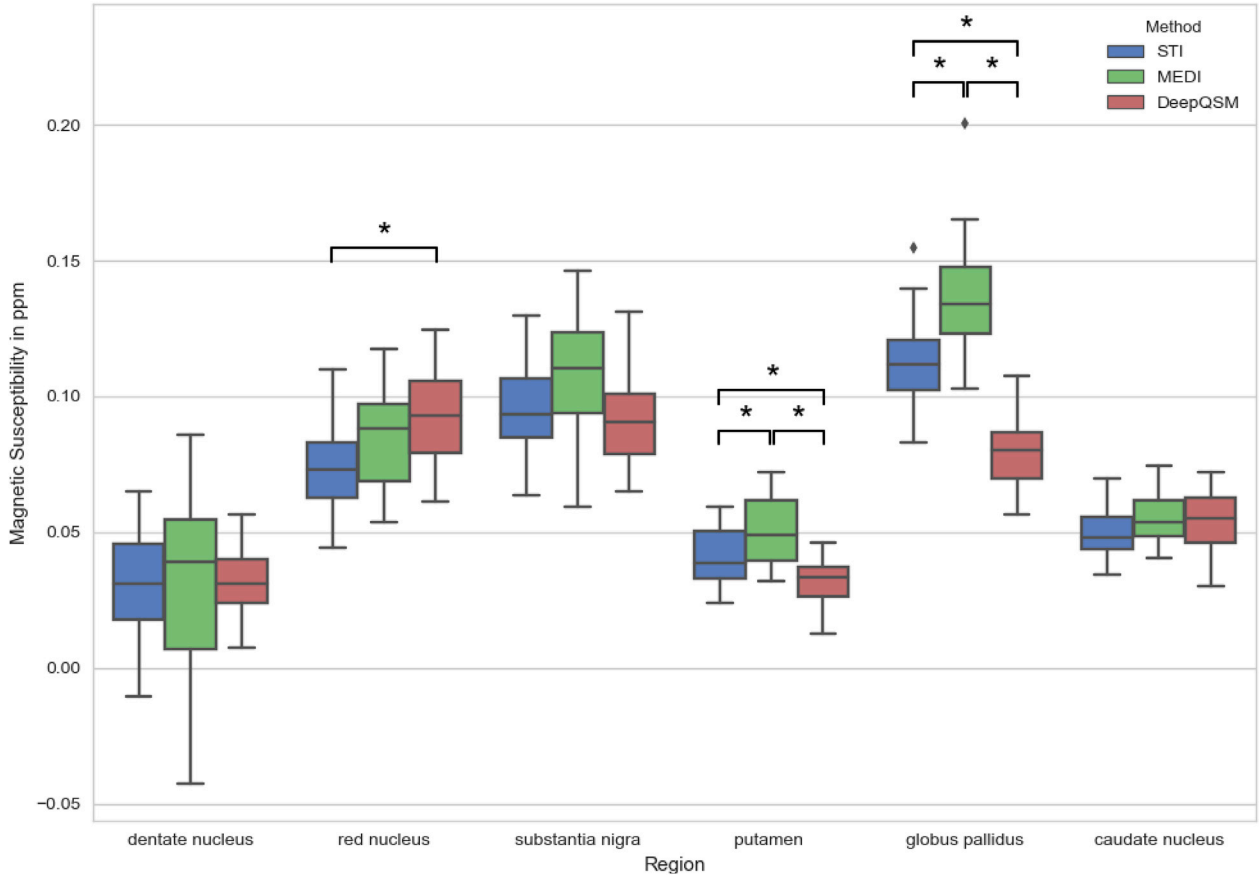

Fig. 6. The box-and-whisker plot shows the results of a region-of-interest analysis across all 27 participants. Differences between DeepQSM and STI are statistically significant in the red nucleus with DeepQSM showing a higher magnetic susceptibility. In the putamen and globus pallidus all methods differ significantly from each other, but DeepQSM shows lower magnetic susceptibilities in comparison to STI and MEDI. In the other regions, the quantitative results are not differing significantly between methods.

diffusion information, could deliver more accurate results in anisotropic white matter regions, because the susceptibility contrast depends on white matter fiber orientation (Li et al., 2012). Utilizing a more sophisticated model for QSM was recently proposed in the QUASAR approach (Schweser and Zivadinov, 2018) and implemented in DEEPOLE that separates the magnetic field into two components originating from different contrast mechanisms and yields an improved susceptibility map accounting for microstructural anisotropy (Jochmann et al., 2019).

5. Conclusions

In summary, we have described the foundations for a new class of QSM inversion algorithms that allow the solution of the QSM inverse problem using a deep convolutional neural network. We show that it is possible to learn the QSM inversion problem from synthetic data describing the known and well-posed forward problem.

Declarations of interest

Authors SB, MB, KO are co-inventors of a patent "Solving the ill-posed quantitative susceptibility mapping inverse problem using deep convolutional neural networks" filed on 29th Dec 2017

Acknowledgements

The authors acknowledge the facilities and scientific and technical assistance of the National Imaging Facility, a National Collaborative Research Infrastructure Strategy (NCRIS) capability, at the Centre for Advanced Imaging, The University of Queensland. KR, MK, and RG acknowledge funding from the following private organisations: Aalborg University Internationalisation foundation, Otto Mønsted foundation, Knud Højgaard Foundation, Danish Tennis Foundation, Nordea Foundation, Julie Damms study-foundation and Oticon foundation. CL acknowledges funding from the Austrian Science Fund (FWF grants KLI523 and P30134). SB acknowledges funding from UQ Postdoctoral Research Fellowship grant and support via an Nvidia hardware grant. MB acknowledges funding from Australian Research Council Future Fellowship grant FT140100865. This research was undertaken with the assistance of resources and services from the Queensland Cyber Infrastructure Foundation (QCIF) and the National Computational Infrastructure, which is supported by the Australian Government. We thank Marlies Hankel and Jake Carroll for enabling the access to the necessary compute capabilities, Joshua Arnold for initial discussions and implementations that laid the foundations of this project and Matthew Cronin for valuable feedback on the bioRxiv preprint.

Appendix A. Supplementary data

Supplementary data to this article can be found online at https://doi.org/10.1016/j.neuroimage.2019.03.060.

References

Abadi, M., Agarwal, A., Barham, P., Brevdo, E., Chen, Z., Citro, C., Corrado, G.S., Davis, A., Dean, J., Devin, M., 2016. Tensorflow: large-scale machine learning on heterogeneous distributed systems. 160304467.

Acosta-Cabronero, J., Betts, M.J., Cardenas-Blanco, A., Yang, S., Nestor, P.J., 2016. In vivo MRI mapping of brain iron deposition across the adult lifespan. J. Neurosci. 36, 364–374. https://doi.org/10.1523/JNEUROSCI.1907-15.2016.

Acosta-Cabronero, J., Cardenas-Blanco, A., Betts, M.J., Butryn, M., Valdes-Herrera, J.P., Galazky, I., Nestor, P.J., 2017. The whole-brain pattern of magnetic susceptibility perturbations in Parkinson's disease. Brain 140, 118–131. https://doi.org/10.1093/brain/aww278.

Acosta-Cabronero, J., Williams, G.B., Cardenas-Blanco, A., Arnold, R.J., Lupson, V., Nestor, P.J., 2013. In vivo quantitative susceptibility mapping (QSM) in alzheimer's disease. PLoS One 8, e81093. https://doi.org/10.1371/journal.pone.0081093.

Anderson, C., Nencka, A., Muftuler, T., Schmainda, K., Koch, K., 2016. Volume-parcellated quantitative susceptibility mapping. In: Proceedings of the Annual Meeting and Exhibition of the International Society for Magnetic Resonance in Medicine. Presented at the ISMRM 2016, Singapore.

Bahrami, K., Shi, F., Rekik, I., Gao, Y., Shen, D., 2017. 7T-guided super-resolution of 3T MRI. Med. Phys. 44, 1661–1677.

Bilgic, B., Pfefferbaum, A., Rohlfing, T., Sullivan, E.V., Adalsteinsson, E., 2012. MRI estimates of brain iron concentration in normal aging using quantitative susceptibility mapping. Neuroimage 59, 2625–2635. https://doi.org/10.1016/j.neuroimage.2011.08.077.

Bollmann, S., Kristensen, M.H., Larsen, M.S., Olsen, M.V., Pedersen, M.J., Østergaard, L.R., O'Brien, K., Langkammer, C., Fazlollahi, A., Barth, M., 2019. SHARQnet – sophisticated harmonic artifact reduction in quantitative susceptibility mapping using a deep convolutional neural network. Z. Med. Phys. ISSN 0939-3889 https://doi.org/10.1016/j.zemedi.2019.01.001.

Brett, M., Hanke, M., Markiewicz, C., Côté, M.-A., McCarthy, P., Ghosh, S., Wassermann, D., Gerhard, S., Halchenko, Y., Larson, E., Lee, G.R., Kastman, E., M.,C., Morency, F.C., moloney, Rokem, A., Cottaar, M., Millman, J., Markello, R., jaeilepp, Cheng, C., Gramfort, A., Vincent, R.D., Bosch, J.J.F. van den, Subramaniam, K., Raamana, P.R., Goncalves, M., Nichols, N., embaker, Basile, 2018. Nipy/Nibabel: 2.3.0. Zenodo. https://doi.org/10.5281/zenodo.1287921.

Burger, H.C., Schuler, C.J., Harmeling, S., 2012. Image denoising: can plain neural networks compete with BM3D?. In: 2012 IEEE Conference on Computer Vision and Pattern Recognition. Presented at the 2012 IEEE Conference on Computer Vision and Pattern Recognition, pp. 2392–2399. https://doi.org/10.1109/CVPR.2012.6247952.

Chatnuntawech, I., McDaniel, P., Cauley, S.F., Gagoski, B.A., Langkammer, C., Martin, A., Grant, P.E., Wald, L.L., Setsompop, K., Adalsteinsson, E., Bilgic, B., 2017. Single-step quantitative susceptibility mapping with variational penalties: single-Step Qsm with Variational Penalties. NMR Biomed. 30, e3570. https://doi.org/10.1002/nbm.3570.

Deistung, A., Schäfer, A., Schweser, F., Biedermann, U., Turner, R., Reichenbach, J.R., 2013. Toward in vivo histology: a comparison of quantitative susceptibility mapping (QSM) with magnitude-, phase-, and R2-imaging at ultra-high magnetic field strength. Neuroimage 65, 299–314. https://doi.org/10.1016/j.neuroimage.2012.09.055.

Deistung, A., Schweser, F., Reichenbach, J.R., 2017. Overview of quantitative susceptibility mapping: overview of quantitative susceptibility mapping. NMR Biomed. 30, e3569. https://doi.org/10.1002/nbm.3569.

Duyn, J.H., 2018. Studying brain microstructure with magnetic susceptibility contrast at high-field. Neuroimage 168, 152–161. https://doi.org/10.1016/j.neuroimage.2017.02.046.

Eskreis-Winkler, S., Deh, K., Gupta, A., Liu, T., Wisnieff, C., Jin, M., Gauthier, S.A., Wang, Y., Spincemaille, P., 2015. Multiple sclerosis lesion geometry in quantitative susceptibility mapping (QSM) and phase imaging: MS Lesions on QSM and Phase. J. Magn. Reson. Imaging 42, 224–229. https://doi.org/10.1002/jmri.24745.

Fan, K., Wei, Q., Wang, W., Chakraborty, A., Heller, K., 2017. InverseNet: Solving Inverse Problems with Splitting Networks. ArXiv171200202 Cs.

Fonov, V., Evans, A.C., Botteron, K., Almli, C.R., McKinstry, R.C., Collins, D.L., 2011. Unbiased average age-appropriate atlases for pediatric studies. Neuroimage 54, 313–327. https://doi.org/10.1016/j.neuroimage.2010.07.033.

Francois, C., 2015. Keras [WWW Document]. https://github.com/fchollet/keras.

Fritzsch, D., Reiss-Zimmermann, M., Trampel, R., Turner, R., Hoffmann, K.-T., Schafer, A., 2014. Seven-tesla magnetic resonance imaging in wilson disease using quantitative susceptibility mapping for measurement of copper accumulation. Investig. Radiol. 49, 299–306. https://doi.org/10.1097/RLI.0000000000000010. May 2014.

Golkov, V., Dosovitskiy, A., Sperl, J.I., Menzel, M.I., Czisch, M., Sämann, P., Brox, T., Cremers, D., 2016. Q-space deep learning: twelve-fold shorter and model-free diffusion MRI scans. IEEE Trans. Med. Imaging 35, 1344–1351. https://doi.org/10.1109/TMI.2016.2551324.

Gorgolewski, K., Burns, C.D., Madison, C., Clark, D., Halchenko, Y.O., Waskom, M.L., Ghosh, S.S., 2011. Nipype: a flexible, lightweight and extensible neuroimaging data processing framework in Python. Front. Neuroinf. 5. https://doi.org/10.3389/fninf.2011.00013.

Grabner, G., Janke, A.L., Budge, M.M., Smith, D., Pruessner, J., Collins, D.L., 2006. Symmetric atlasing and model based segmentation: an application to the hippocampus in older adults. In: Med. Image Comput. Comput.-Assist. Interv. MICCAI Int. Conf. Med. Image Comput. Comput.-Assist. Interv, vol. 9, pp. 58–66.

Gregor, K., LeCun, Y., 2010. Learning fast approximations of sparse coding. In: Presented at the 27th International Conference on Machine Learning, ICML 2010.

Grodzki, D.M., Jakob, P.M., Heismann, B., 2012. Ultrashort echo time imaging using pointwise encoding time reduction with radial acquisition (PETRA). Magn. Reson. Med. 67, 510–518. https://doi.org/10.1002/mrm.23017.

Haacke, E.M., Xu, Y., Cheng, Y.-C.N., Reichenbach, J.R., 2004. Susceptibility weighted imaging (SWI). Magn. Reson. Med. 52, 612–618. https://doi.org/10.1002/mrm.20198.

Haase, A., Frahm, J., Matthaei, D., Hanicke, W., Merboldt, K.-D., 1986. FLASH imaging. Rapid NMR imaging using low flip-angle pulses. J. Magn. Reson. 1969 (67), 258–266. https://doi.org/10.1016/0022-2364(86)90433-6.

Heber, S., Tinauer, C., Bollmann, S., Ropele, S., Langkammer, C., 2019. Deep quantitative susceptibility mapping by combined background field removal and dipole inversion. In: Proc. Intl. Soc. Mag. Reson. Med. 27. Presented at the ISMRM, Montreal, Canada.

Hornik, K., 1991. Approximation capabilities of multilayer feedforward networks. Neural Network. 4, 251–257. https://doi.org/10.1016/0893-6080(91)90009-T.

Hunter, J.D., 2007. Matplotlib: a 2D graphics environment. Comput. Sci. Eng. 9, 90–95. https://doi.org/10.1109/MCSE.2007.55.

Janke, A.L., Ullmann, J.F.P., 2015. Robust methods to create ex vivo minimum deformation atlases for brain mapping. Methods, Spatial Mapp. Multi-Modal Data Neurosci. 73, 18–26. https://doi.org/10.1016/j.ymeth.2015.01.005.

Jin, K.H., McCann, M.T., Froustey, E., Unser, M., 2017. Deep convolutional neural network for inverse problems in imaging. IEEE Trans. Image Process. 26, 4509–4522. https://doi.org/10.1109/TIP.2017.2713099.

Jochmann, T., Haueisen, J., Zivadinov, R., Schweser, F., 2019. U2-Net for DEEPOLE QUASAR–A physics-informed deep convolutional neural network that disentangles MRI phase contrast mechanisms. In: International Society of Magnetic Resonance in Medicine (ISMRM) 27th Annual Meeting. Presented at the International Society of Magnetic Resonance in Medicine (ISMRM) 27th Annual Meeting, Montreal, Canada.

Jones, E., Oliphant, T., Peterson, P., 2001. SciPy: Open Source Scientific Tools for Python.

Kim, J., Kwon Lee, J., Mu Lee, K., 2016. Accurate image super-resolution using very deep convolutional networks. In: Proceedings of the IEEE Conference on Computer Vision and Pattern Recognition, pp. 1646–1654.

Kingma, D., Ba, J., 2014. Adam: a method for stochastic optimization. 14126980.

Langkammer, C., Bredies, K., Poser, B.A., Barth, M., Reishofer, G., Fan, A.P., Bilgic, B., Fazekas, F., Mainero, C., Ropele, S., 2015. Fast quantitative susceptibility mapping using 3D EPI and total generalized variation. Neuroimage 111, 622–630. https://doi.org/10.1016/j.neuroimage.2015.02.041.

Langkammer, C., Pirpamer, L., Seiler, S., Deistung, A., Schweser, F., Franthal, S., Homayoon, N., Katschnig-Winter, P., Koegl-Wallner, M., Pendl, T., Stoegerer, E.M., Wenzel, K., Fazekas, F., Ropele, S., Reichenbach, J.R., Schmidt, R., Schwingenschuh, P., 2016. Quantitative susceptibility mapping in Parkinson's disease. PLoS One 11 e0162460. https://doi.org/10.1371/journal.pone.0162460.

Langkammer, C., Schweser, F., Krebs, N., Deistung, A., Goessler, W., Scheurer, E., Sommer, K., Reishofer, G., Yen, K., Fazekas, F., Ropele, S., Reichenbach, J.R., 2012. Quantitative susceptibility mapping (QSM) as a means to measure brain iron? A post mortem validation study. Neuroimage 62, 1593–1599. https://doi.org/10.1016/j.neuroimage.2012.05.049.

Langkammer, C., Schweser, F., Shmueli, K., Kames, C., Li, X., Guo, L., Milovic, C., Kim, J., Wei, H., Bredies, K., Buch, S., Guo, Y., Liu, Z., Meineke, J., Rauscher, A., Marques, J.P., Bilgic, B., 2018. Quantitative susceptibility mapping: report from the 2016 reconstruction challenge: QSM Reconstruction Challenge 2016. Magn. Reson. Med. 79, 1661–1673. https://doi.org/10.1002/mrm.26830.

Li, W., Avram, A.V., Wu, B., Xiao, X., Liu, C., 2014. Integrated Laplacian-based phase unwrapping and background phase removal for quantitative susceptibility mapping. NMR Biomed. 27, 219–227. https://doi.org/10.1002/nbm.3056.

Li, W., Wang, N., Yu, F., Han, H., Cao, W., Romero, R., Tantiwongkosi, B., Duong, T.Q., Liu, C., 2015. A method for estimating and removing streaking artifacts in quantitative susceptibility mapping. Neuroimage 108, 111–122. https://doi.org/10.1016/j.neuroimage.2014.12.043.

Li, W., Wu, B., Avram, A.V., Liu, C., 2012. Magnetic susceptibility anisotropy of human brain in vivo and its molecular underpinnings. Neuroimage 59, 2088–2097. https://doi.org/10.1016/j.neuroimage.2011.10.038.

Li, W., Wu, B., Liu, C., 2011. Quantitative susceptibility mapping of human brain reflects spatial variation in tissue composition. Neuroimage 55, 1645–1656. https://doi.org/10.1016/j.neuroimage.2010.11.088.

Liu, C., 2010. Susceptibility tensor imaging. Magn. Reson. Med. Off. J. Soc. Magn. Reson. Med. Soc. Magn. Reson. Med. 63, 1471–1477. https://doi.org/10.1002/mrm.22482.

Liu, C., Li, W., Tong, K.A., Yeom, K.W., Kuzminski, S., 2015. Susceptibility-weighted imaging and quantitative susceptibility mapping in the brain. J. Magn. Reson. Imaging 42, 23–41. https://doi.org/10.1002/jmri.24768.

Liu, T., Liu, J., de Rochefort, L., Spincemaille, P., Khalidov, I., Ledoux, J.R., Wang, Y., 2011. Morphology enabled dipole inversion (MEDI) from a single-angle acquisition: comparison with COSMOS in human brain imaging. Magn. Reson. Med. 66, 777–783. https://doi.org/10.1002/mrm.22816.

Liu, T., Spincemaille, P., de Rochefort, L., Kressler, B., Wang, Y., 2009. Calculation of susceptibility through multiple orientation sampling (COSMOS): a method for conditioning the inverse problem from measured magnetic field map to susceptibility source image in MRI. Magn. Reson. Med. 61, 196–204. https://doi.org/10.1002/mrm.21828.

Liu, T., Surapaneni, K., Lou, M., Cheng, L., Spincemaille, P., Wang, Y., 2012a. Cerebral microbleeds: burden assessment by using quantitative susceptibility mapping. Radiology 262, 269–278. https://doi.org/10.1148/radiol.11110251.

Liu, T., Wisnieff, C., Lou, M., Chen, W., Spincemaille, P., Wang, Y., 2013. Nonlinear formulation of the magnetic field to source relationship for robust quantitative susceptibility mapping. Magn. Reson. Med. 69, 467–476. https://doi.org/10.1002/mrm.24272.

Liu, T., Xu, W., Spincemaille, P., Avestimehr, A.S., Wang, Y., 2012b. Accuracy of the morphology enabled dipole inversion (MEDI) algorithm for quantitative susceptibility mapping in MRI. IEEE Trans. Med. Imaging 31, 816–824. https://doi.org/10.1109/TMI.2011.2182523.

McCann, M.T., Jin, K.H., Unser, M., 2017. Convolutional neural networks for inverse problems in imaging: a review. IEEE Signal Process. Mag. 34, 85–95. https://doi.org/10.1109/MSP.2017.2739299.

McDonagh, S., Hou, B., Kamnitsas, K., Oktay, O., Alansary, A., Kainz, B., 2017. Context-sensitive super-resolution for fast fetal magnetic resonance imaging. 170300035.

Oktay, O., Bai, W., Lee, M., Guerrero, R., Kamnitsas, K., Caballero, J., Marvao, A. de, Cook, S., O'Regan, D., Rueckert, D., 2016. Multi-input cardiac image super-resolution using convolutional neural networks. Medical Image Computing and Computer-Assisted Intervention – MICCAI 2016. Presented at the International Conference on Medical Image Computing and Computer-Assisted Intervention. Springer, Cham, pp. 246–254. https://doi.org/10.1007/978-3-319-46726-9_29.

Oliphant, T.E., 2015. Guide to NumPy, second ed. CreateSpace Independent Publishing Platform, USA.

Paige, C.C., Saunders, M.A., 1982. LSQR: an algorithm for sparse linear equations and sparse least squares. ACM Trans. Math Software 8, 43–71. https://doi.org/10.1145/355984.355989.

Reichenbach, J.R., Venkatesan, R., Yablonskiy, D.A., Thompson, M.R., Lai, S., Haacke, E.M., 1997. Theory and application of static field inhomogeneity effects in gradient-echo imaging. J. Magn. Reson. Imaging 7, 266–279. https://doi.org/10.1002/jmri.1880070203.

Robinson, S.D., Dymerska, B., Bogner, W., Barth, M., Zaric, O., Goluch, S., Grabner, G., Deligianni, X., Bieri, O., Trattnig, S., 2017. Combining phase images from array coils using a short echo time reference scan (COMPOSER). Magn. Reson. Med. 77, 318–327. https://doi.org/10.1002/mrm.26093.

Ronneberger, O., Fischer, P., Brox, T., 2015. U-net: convolutional networks for biomedical image segmentation. Medical Image Computing and Computer-Assisted Intervention – MICCAI 2015, Lecture Notes in Computer Science. Presented at the International Conference on Medical Image Computing and Computer-Assisted Intervention. Springer, Cham, pp. 234–241. https://doi.org/10.1007/978-3-319-24574-4_28.

Rossum, G., 1995. Python Reference Manual. CWI. Centre for Mathematics and Computer Science, Amsterdam, The Netherlands, The Netherlands.

Schlemper, J., Caballero, J., Hajnal, J.V., Price, A., Rueckert, D., 2017. A Deep Cascade of Convolutional Neural Networks for MR Image Reconstruction. 170300555.

Schweser, F., Deistung, A., Lehr, B.W., Reichenbach, J.R., 2011. Quantitative imaging of intrinsic magnetic tissue properties using MRI signal phase: an approach to in vivo brain iron metabolism? Neuroimage 54, 2789–2807. https://doi.org/10.1016/j.neuroimage.2010.10.070.

Schweser, F., Deistung, A., Lehr, B.W., Reichenbach, J.R., 2010. Differentiation between diamagnetic and paramagnetic cerebral lesions based on magnetic susceptibility mapping. Med. Phys. 37, 5165–5178. https://doi.org/10.1118/1.3481505.

Schweser, F., Deistung, A., Reichenbach, J.R., 2016. Foundations of MRI phase imaging and processing for quantitative susceptibility mapping (QSM). Z. Med. Phys. 26, 6–34. https://doi.org/10.1016/j.zemedi.2015.10.002.

Schweser, F., Sommer, K., Deistung, A., Reichenbach, J.R., 2012. Quantitative susceptibility mapping for investigating subtle susceptibility variations in the human brain. Neuroimage 62, 2083–2100. https://doi.org/10.1016/j.neuroimage.2012.05.067.

Schweser, F., Zivadinov, R., 2018. Quantitative susceptibility mapping (QSM) with an extended physical model for MRI frequency contrast in the brain: a proof-of-concept of quantitative susceptibility and residual (QUASAR) mapping. NMR Biomed. 31, e3999. https://doi.org/10.1002/nbm.3999.

Seabold, S., Perktold, J., 2010. Statsmodels: econometric and statistical modeling with Python. In: Proceedings of the 9th Python in Science Conference.

Shen, D., Wu, G., Suk, H.-I., 2017. Deep learning in medical image analysis. Annu. Rev. Biomed. Eng. 19, 221–248. https://doi.org/10.1146/annurev-bioeng-071516-044442.

Shmueli, K., de Zwart, J.A., van Gelderen, P., Li, T.-Q., Dodd, S.J., Duyn, J.H., 2009. Magnetic susceptibility mapping of brain tissue in vivo using MRI phase data. Magn. Reson. Med. 62, 1510–1522. https://doi.org/10.1002/mrm.22135.

Smith, S.M., 2002. Fast robust automated brain extraction. Hum. Brain Mapp. 17, 143–155. https://doi.org/10.1002/hbm.10062.

Srivastava, N., Hinton, G.E., Krizhevsky, A., Sutskever, I., Salakhutdinov, R., 2014. Dropout: a simple way to prevent neural networks from overfitting. J. Mach. Learn. Res. 15, 1929–1958.

Tukey, J.W., 1949. Comparing individual means in the analysis of variance. Biometrics 5, 99–114. https://doi.org/10.2307/3001913.

van Bergen, J.M.G., Hua, J., Unschuld, P.G., Lim, I.A.L., Jones, C.K., Margolis, R.L., Ross, C.A., van Zijl, P.C.M., Li, X., 2016. Quantitative susceptibility mapping suggests altered brain iron in premanifest Huntington disease. Am. J. Neuroradiol. 37, 789–796. https://doi.org/10.3174/ajnr.A4617.

Walt, S. van der, Schönberger, J.L., Nunez-Iglesias, J., Boulogne, F., Warner, J.D., Yager, N., Gouillart, E., Yu, T., 2014. scikit-image: image processing in Python. PeerJ 2, e453. https://doi.org/10.7717/peerj.453.

Wang, Y., Spincemaille, P., Liu, Z., Dimov, A., Deh, K., Li, J., Zhang, Y., Yao, Y., Gillen, K.M., Wilman, A.H., Gupta, A., Tsiouris, A.J., Kovanlikaya, I., Chiang, G.C.-Y., Weinsaft, J.W., Tanenbaum, L., Chen, W., Zhu, W., Chang, S., Lou, M., Kopell, B.H., Kaplitt, M.G., Devos, D., Hirai, T., Huang, X., Korogi, Y., Shtilbans, A., Jahng, G.-H., Pelletier, D., Gauthier, S.A., Pitt, D., Bush, A.I., Brittenham, G.M., Prince, M.R., 2017. Clinical quantitative susceptibility mapping (QSM): biometal imaging and its emerging roles in patient care: clinical QSM Biometals. J. Magn. Reson. Imaging 46, 951–971. https://doi.org/10.1002/jmri.25693.

Waskom, M., Botvinnik, Olga, Drew, O'Kane, Paul, Hobson, Lukauskas, Saulius, Gemperline, David C., Augspurger, Tom, Halchenko, Yaroslav, Cole, John B., Warmenhoven, Jordi, de Ruiter, Julian, Cameron, Pye, Stephan, Hoyer, Jake, Vanderplas, Santi, Villalba, Gero, Kunter, Eric, Quintero, Pete, Bachant, Marcel, Martin, Kyle, Meyer, Alistair, Miles, Yoav, Ram, Tal, Yarkoni, Mike, Lee Williams, Constantine, Evans, Clark, Fitzgerald, Brian, Chris, Fonnesbeck, Lee, Antony, Qalieh, Adel, 2017. Mwaskom/Seaborn: v0.8.1 (September 2017). Zenodo. https://doi.org/10.5281/zenodo.883859.

Wharton, S., Bowtell, R., 2015. Effects of white matter microstructure on phase and susceptibility maps. Magn. Reson. Med. 73, 1258–1269. https://doi.org/10.1002/mrm.25189.

Wharton, S., Bowtell, R., 2010. Whole-brain susceptibility mapping at high field: a comparison of multiple- and single-orientation methods. Neuroimage 53, 515–525. https://doi.org/10.1016/j.neuroimage.2010.06.070.

Wharton, S., Schäfer, A., Bowtell, R., 2010. Susceptibility mapping in the human brain using threshold-based k-space division. Magn. Reson. Med. 63, 1292–1304. https://doi.org/10.1002/mrm.22334.

Wisnieff, C., Ramanan, S., Olesik, J., Gauthier, S., Wang, Y., Pitt, D., 2015. Quantitative susceptibility mapping (QSM) of white matter multiple sclerosis lesions: interpreting positive susceptibility and the presence of iron. Magn. Reson. Med. 74, 564–570. https://doi.org/10.1002/mrm.25420.

Wu, Z., He, H., Sun, Y., Du, Y., Zhong, J., 2017. High resolution myelin water imaging incorporating local tissue susceptibility analysis. Magn. Reson. Imaging 42, 107–113. https://doi.org/10.1016/j.mri.2017.06.005.

Xu, L., Ren, J.S., Liu, C., Jia, J., 2014. Deep convolutional neural network for image deconvolution. In: Advances in Neural Information Processing Systems, pp. 1790–1798.

Yablonskiy, D.A., Sukstanskii, A.L., 2015. Generalized Lorentzian Tensor Approach (GLTA) as a biophysical background for quantitative susceptibility mapping. Magn. Reson. Med. 73, 757–764. https://doi.org/10.1002/mrm.25538.

Yao, B., Li, T.-Q., Gelderen, P. van, Shmueli, K., de Zwart, J.A., Duyn, J.H., 2009. Susceptibility contrast in high field MRI of human brain as a function of tissue iron content. Neuroimage 44, 1259–1266. https://doi.org/10.1016/j.neuroimage.2008.10.029.

Yoon, J., Gong, E., Chatnuntawech, I., Bilgic, B., Lee, Jingu, Jung, W., Ko, J., Jung, H., Setsompop, K., Zaharchuk, G., Kim, E.Y., Pauly, J., Lee, Jongho, 2018. Quantitative susceptibility mapping using deep neural network: QSMnet. Neuroimage 179, 199–206. https://doi.org/10.1016/j.neuroimage.2018.06.030.

Yushkevich, P.A., Piven, J., Hazlett, H.C., Smith, R.G., Ho, S., Gee, J.C., Gerig, G., 2006. User-guided 3D active contour segmentation of anatomical structures: significantly improved efficiency and reliability. Neuroimage 31, 1116–1128. https://doi.org/10.1016/j.neuroimage.2006.01.015.

Zhang, Y., Gauthier, S.A., Gupta, A., Comunale, J., Chia-Yi Chiang, G., Zhou, D., Chen, W., Giambrone, A.E., Zhu, W., Wang, Y., 2016. Longitudinal change in magnetic susceptibility of new enhanced multiple sclerosis (MS) lesions measured on serial quantitative susceptibility mapping (QSM). J. Magn. Reson. Imaging 44, 426–432. https://doi.org/10.1002/jmri.25144.

Zhu, B., Liu, J.Z., Cauley, S.F., Rosen, B.R., Rosen, M.S., 2018. Image reconstruction by domain-transform manifold learning. Nature 555, 487–492. https://doi.org/10.1038/nature25988.